

Optomechanical quantum bus for donor spins in silicon

Henri Lyyra,^{1,2,*} Cliona Shakespeare,¹ Simeoni Ahopelto,¹ Teemu Loippo,¹ Alberto Hijano,¹ Reetu Inkilä,¹ Pyry Runko,¹ Tero T. Heikkilä,¹ and Juha T. Muhonen^{1,†}

¹*Department of Physics and Nanoscience Center, P.O. Box 35,
University of Jyväskylä, FI-40014 University of Jyväskylä, Finland*

²*Department of Mechanical and Materials Engineering,
University of Turku, Turun yliopisto FI-20014, Finland*

Silicon is the foundation of current information technology, and also a very promising platform for the future quantum information technology as silicon-based qubits exhibit some of the longest coherence times in solid-state. At the same time, silicon is the underlying material for advanced photonics activity and photonics structures in silicon can be used to define optomechanical cavities where the vibrations of nanoscale mechanical resonators can be probed down to the quantum level with laser light. Here, we propose to bring all these developments together by coupling silicon donor spins into optomechanical structures. We show theoretically and numerically that this allows telecom wavelength optical readout of the spin-qubits and implementing high-fidelity entangling two-qubit gates between donor spins that are spatially separated by tens of micrometers. We present an optimized geometry of the proposed device and discuss with the help of numerical simulations the predicted performance of the proposed quantum bus. We analyze the optomechanical spin readout fidelity find the optimal donor species for the strain and magnetic field gradient coupling.

I. INTRODUCTION

Conventional semiconductor electronics is built on tailoring silicon's electronic properties by introducing group-V donor atoms. The extensive industrial expertise in this field, coupled with the atomic-scale nature of donor spin qubits, positions them as a natural candidate for the quantum successor to classical bits. Indeed, one of the first scalable quantum computer proposals — the famous Kane quantum computer [1] — relied on the nuclear spin qubits of individual phosphorus atoms. Ever since Kane's seminal paper, the progress towards a donor spin-based silicon quantum computer has been promising [2–4]. In isotopically purified silicon, coherence times of 1.1 ms have been demonstrated with the donor electron spin qubits [5], and these can be even further prolonged by dressing the qubits with a microwave drive [6]. Furthermore, for phosphorus nuclear spin, the coherence time can be prolonged with dynamical decoupling to 30 seconds, a promising demonstration of a quantum memory [5]. Single-qubit logical operations with gate fidelities above 99.9 % have also been demonstrated with the electron spin qubits. [7].

In Kane's original idea, two nuclear spin qubits would interact using the exchange interaction of two electron spins as a mediator, allowing performing 2-qubit quantum gates with the neighboring qubits. However, in order to get strong enough coupling, the donors have to be implanted with precision of 20 - 30 nm in the original proposal, posing already severe challenges for the integration of the control and measurement electronics for multi-qubit quantum processors. Later, it was realized

that the multi-valley nature of silicon gives rise to atomic-scale oscillations in the exchange energy [8], making the multi-qubit implementation even more challenging.

Despite a recent promising three-qubit demonstration with donor spins [9] and entangling two donor spin-qubits [10], a fully scalable interaction between donor spins is yet to be demonstrated, although several theoretical suggestions have been made [11, 12]. Another challenge currently limiting the scalability of donor spin-based silicon quantum computers is the readout of the qubit states. Although the information could be processed even at 4 K, the reservoir tunneling readout currently in use forces operating at millikelvin temperatures and high magnetic fields [2].

Here we propose to solve these issues with a new quantum hybrid system coupling the donor spins to an optomechanical platform in order to enable optical readout of the spins as well as a phononic pathway to couple the spins to each other. The platform is inherently scalable as it leverages the existing framework of silicon photonics by transducing the spin information to telecom range photons. In addition, the architecture allows for local coherent spin-spin couplings via the mechanical elements. We describe a detailed proposal for silicon based quantum computing utilizing existing optomechanical devices and discuss in detail the usage of the mechanical mode for two-qubit gates. In addition a crucial ingredient for our proposal is the use of a microwave dressed spin state that offers multiple advantages. We give a through comparison of the general features of the dressed coupling compared to the bare coupling in another paper [13].

Optomechanical systems have shown their promise as quantum transducers in multiple different settings. Due to the ability to couple mechanical motion to many different degrees of freedom, there are active projects developing optomechanical platforms for quantum transduction between different quantum states [14, 15], such

* hesaly@utu.fi

† juha.t.muhonen@jyu.fi

as between microwave and optical photons [16] or between defect qubits and optical photons [17]. Information can also be stored in mechanical resonators: There are demonstrations of acoustic systems with quality factors above 10^{10} [18] and using them as quantum memories for superconducting qubits [19, 20]. Besides quantum technologies, high fidelity state preparation and readout of a semi-macroscopic mechanical resonator could help answer some very foundational questions about quantum physics, for example testing the continuous spontaneous collapse models [21, 22] and gravitational decoherence [23].

In this paper, we propose and analyze the performance of an optomechanical quantum bus that exploits mechanical resonators for optical spin-qubit readout and two-qubit gates. Our proposed platform combines the recent advancements of high-precision single-ion implantation [24–27], high-fidelity control of donor spin-qubits [6], and nanofabrication of optomechanical resonators [28]. The donors implanted in isotopically purified silicon couple to an optomechanical sliced photonic crystal nanobeam resonator. The fully silicon on-chip design simplifies the fabrication and scalability compared to architectures that depend on several electrical lines to each qubit. Furthermore, the telecom wavelength optical readout enables quantum information processing at higher temperatures and opens the possibility for connecting the donor spins with photonic communication networks and distributed quantum computing. If the mechanical resonator is cooled down to its ground state, the proposed quantum bus can be also used as a testbed to push the boundaries between the quantum and classical worlds.

The paper is organised as follows: section II gives an overview of the proposed platform, section III discusses spin readout via changes in the mechanical resonance frequency, section IV discusses the spin-spin coupling via the phonon system and section V gives a concrete proposal on the implementation and achievable spin-phonon coupling strengths. Especially we focus on the coherence and fidelity properties as well as the requirements for donor placing which we show are within reach of current implantation technology.

II. OVERVIEW OF THE HYBRID SYSTEM

Our proposed platform for the optomechanical quantum bus consists of multiple interacting quantum systems, illustrated in Fig. 1. The coupling between the spin and the mechanical resonator can be realized using either a magnetic field gradient or the innate strain coupling. We model the details of the achievable coupling in Sec. V A. Both mechanisms lead to a mechanical displacement-dependent energy splitting of the qubit levels, i.e., to an interaction Hamiltonian proportional to σ_z , where σ is the Pauli spin matrix (taking z as the quantization axis). However, to map the qubit spin to the resonator the interaction should involve σ_x instead.

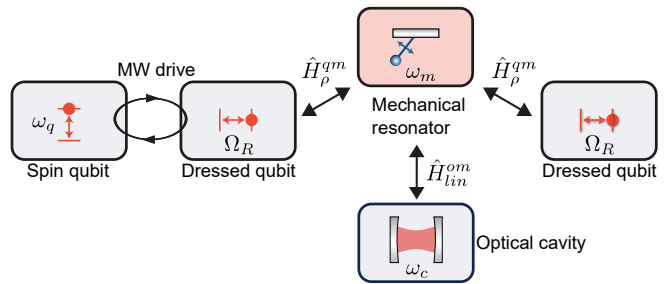


FIG. 1: Schematic of the optomechanical quantum bus. The dressed qubit’s state affects the resonance frequency of the mechanical resonator. The mechanical displacement modulates the resonance frequency of the optical cavity. The spin-dependent mechanical frequency shifts can then be detected by measuring the noise imprinted on the phase quadrature of the light escaping from the cavity. Bringing two spin-qubits near resonance with the resonator allows logical two-qubit operations for spatially separated donor spins. The parameters are discussed in the main text.

Moreover, our aim is to achieve active control over the spin-mechanical interaction, such that it can be turned on and off at will. Both requirements can be addressed by applying a microwave drive resonant with the qubit transition frequency [13]. This drive ‘dresses’ the qubit [6], transforming its eigenstates. In the new dressed basis, the qubit energy splitting is proportional to the microwave drive strength, and hence can be brought in resonance with the mechanical resonance frequencies of typical flexural modes of a micron-scale silicon beams. In this dressed frame the interaction between the mechanical resonator and the spin is proportional to σ_x .

For the optical side, the coupling is realized through a cavity-optomechanical system: the mechanical movement changes the resonance frequency of an optical cavity. Here, we specifically model the case where we work with an optomechanical system in the non-resolved sideband limit, where the phase of the light escaping the cavity contains information on the instantaneous position of the resonator. We show specific geometries in Sec. V. The modelled optical wavelength is the optical telecommunication band at 1550 nm.

This system can then be utilized in two different regimes. In the dispersive regime (i.e., when the dressed state is detuned from the mechanical resonator) the spin state can be read out optically by observing changes in the mechanical resonance frequency, analogously on how superconducting qubits are read out via changes in the resonance frequency of a microwave resonator [29]. Notably, this gives a quantum non-demolition readout mechanism. This is in contrast to direct optical readout as used with e.g. NV-centers in diamond. On the other hand, tuning the spins in resonance with the mechanical resonator would then allow coherent state transfer between the mechanical resonator and the spin. This

regime could then be used for both coherent coupling between separate spins via phonons, and to possibly coherently couple the spin state to the light field via the optomechanical system. The direct spin-phonon-spin interaction is however hard to realize with the low frequency mechanical modes we consider here as they tend to have a finite thermal occupancy. Hence, instead we note that a two-qubit gate can also be accomplished in the dispersive regime, limiting the effects of the finite temperature of the mechanical bus. This is discussed in detail in Sec. IV.

A. Dressed frame coupling

Here we present the Hamiltonian formulation of coupling the spin qubit and the mechanical resonator. For clarity, we neglect the hyperfine interaction between the donor bound electron spin and the donor nuclear spin. Our qubit system here is the donor bound electron spin.

We start with the canonical spin qubit Hamiltonian and assume a static magnetic field B_0 is applied. The energy levels of the electron spin states are separated by the Zeeman splitting $\gamma_e B_0$, where $\gamma_e := \frac{g_e \mu_B}{\hbar}$ is the electron gyromagnetic ratio, g_e is the electron g -factor, μ_B is the Bohr magneton. If we then add a mechanical resonator whose displacement $\hat{a}^\dagger + \hat{a}$ modulates the Zeeman splitting, the Hamiltonian of the total qubit-resonator system reads

$$\frac{\hat{H}^{qm}}{\hbar} = \frac{1}{2} [\gamma_e B_0 \hat{\sigma}_z + 2\omega_m \hat{a}^\dagger \hat{a} + \lambda \hat{\sigma}_z (\hat{a}^\dagger + \hat{a})], \quad (1)$$

where we have shifted the mechanical resonator's ground state energy to zero by omitting the zero-point fluctuation term, ω_m is the mechanical resonance frequency, and \hat{a}^\dagger and \hat{a} are the creation and annihilation operators for the mechanical resonator mode phonons, respectively. The coupling strength λ between the resonator and the spin qubit depends on the coupling mechanism, donor species, and device design, see Sec. V A for details.

The spin qubit states can be controlled by applying an AC electromagnetic field (drive in the following) with a magnetic component orthogonal to the applied DC field ($\vec{B}_1 \perp \vec{B}_0$) oscillating at the MW frequency ν_{MW} . The Hamiltonian with the oscillating magnetic field (which we model as a classical drive) can be written as

$$\frac{\hat{H}^{qm}}{\hbar} = \frac{1}{2} [\gamma_e B_0 \hat{\sigma}_z + \gamma_e B_1 \cos(2\pi\nu_{MW}t) \hat{\sigma}_x + 2\omega_m \hat{a}^\dagger \hat{a} + \lambda \hat{\sigma}_z (\hat{a}^\dagger + \hat{a})]. \quad (2)$$

When ν_{MW} is in resonance with the Zeeman splitting, the drive starts driving the spin transition, causing coherent oscillations between the states $|\downarrow\rangle$ and $|\uparrow\rangle$ at the Rabi frequency $\Omega_R := \frac{1}{2}\gamma_e B_1$. Here, $|\downarrow\rangle$ and $|\uparrow\rangle$ are the eigenstates of $\hat{\sigma}_z$.

By moving into the coordinates rotating with the MW drive and applying the change of basis, Eq. (2) simplifies

into

$$\frac{\hat{H}_\rho^{qm}}{\hbar} = \frac{1}{2} [\Omega_R \hat{\sigma}_z + \Delta\nu \hat{\sigma}_x + 2\omega_m \hat{a}^\dagger \hat{a} - \lambda \hat{\sigma}_x (\hat{a}^\dagger + \hat{a})], \quad (3)$$

where the original eigenstates of the bare qubit $|\downarrow\rangle$ and $|\uparrow\rangle$ are now the eigenstates of $\hat{\sigma}_x$ in these coordinates, and we have denoted the MW detuning as $\Delta\nu := \nu_{MW} - \gamma_e B_0$.

If the qubit is driven resonantly, $\Delta\nu = 0$, we get a new qubit, *the dressed qubit* with Ω_R as its eigenfrequency. Previous experiments with silicon donor spins have shown that the dressing detaches the qubit from the low frequency noise, and can prolong the coherence times by one order of magnitude giving coherence times for $T_{2\rho}^* = 2.4$ ms, and $T_{2\rho}^{Hahn} = 9$ ms for a ^{31}P donor in silicon [6]. Importantly, since the eigenfrequency Ω_R is tuned by the intensity of the MW drive, the qubit can be brought into and out of resonance with a mechanical resonator by tuning the microwave drive, hence giving precise control of the interaction time between the qubit and the mechanical resonator. Also, the eigenstates of the dressed qubit are perpendicular to the bare spin-qubit, which allows for the transverse coupling with the mechanical resonator.

Finally, if $\Delta\nu = 0$ and we apply the rotating wave approximation (RWA), we have the standard Jaynes-Cummings Hamiltonian between the dressed qubit and the mechanical resonator

$$\frac{\hat{H}_{\rho,RWA}^{qm}}{\hbar} = \frac{1}{2} [\Omega_R \hat{\sigma}_z + 2\omega_m \hat{a}^\dagger \hat{a} - \lambda (\hat{\sigma}_- \hat{a}^\dagger + \hat{\sigma}_+ \hat{a})]. \quad (4)$$

In our numerical simulations, we omit the RWA and use the Hamiltonian of Eq. (3) to avoid the influence of any unnecessary assumptions in our analysis. However, the RWA Hamiltonian in Eq. (4) combined with other assumptions is a useful tool to provide intuition on why and how the quantum bus implements qubit readout and two-qubit gates, as we discuss in Sec. III and Sec. IV, respectively.

B. The optomechanical resonator

For completeness, we describe here shortly the optomechanical interaction. Although it is not the main component in the modeling we present, it is crucial to understand what is our measured quantity.

The key ingredient of our proposed quantum bus is the ability of mechanical resonators to interact simultaneously with a plethora of different physical systems via changes of displacement, strain, or changes in the device geometry. Especially the field of optomechanics relies on the mechanical motion of a resonator modifying the resonance frequency ω_c of an optical cavity. This optomechanical interaction can among other things be exploited to monitor and control the mechanical oscillator, which

is an integral part of our optomechanical quantum bus. In coordinates rotating at the laser frequency ω_L and linearizing the optomechanical interaction term, the optomechanical Hamiltonian can be written in the simple form

$$\begin{aligned} \frac{\hat{H}_{lin}^{om}}{\hbar} = & \omega_m \hat{a}^\dagger \hat{a} - \Delta_{CL} \delta \hat{b}^\dagger \hat{b} \\ & - g_0 \sqrt{\langle n_{cav} \rangle} (\hat{a}^\dagger + \hat{a}) (\delta \hat{b}^\dagger + \delta \hat{b}) \end{aligned} \quad (5)$$

where $\Delta_{CL} = \omega_c - \omega_L$ is the detuning between the optical cavity and the laser drive, $\delta \hat{b}^\dagger$ and $\delta \hat{b}$ are the photon number fluctuation creation and annihilation operators, g_0 is the single photon optomechanical coupling strength, and $\langle n_{cav} \rangle$ is the average photon number inside the cavity [30]. The interaction term in Eq. (5) couples the displacement operator of the mechanical resonator to the phase quadrature of the photon field. This imprints the mechanical motion to the phase noise of the light leaking out of the optical cavity. Specifically our observable is the symmetrized power spectral density of the mechanical motion [31], as we detail below.

From now on, we will mostly neglect the optomechanical interaction, and we concentrate only on the spin-mechanics part of the optomechanical quantum bus, described by the Hamiltonian in Eq. (3). In the next two sections, we will discuss how the described quantum bus can be used for optomechanical readout and controlled two-qubit gates for donor spin qubits in silicon.

III. SPIN READOUT VIA CHANGES IN THE MECHANICAL RESONANCE FREQUENCY

A. Dispersive limit

To get intuition of how and why the optomechanical spin-qubit readout works, let us first consider the qubit-mechanics Hamiltonian under the RWA in Eq. (4). Now, we consider the *dispersive regime* where the qubit and the mechanical resonator do not exchange energy by assuming $\lambda \ll 2|\Omega_R - \omega_m| =: 2\Delta_R$ and $n_{th} := \langle \hat{a}^\dagger \hat{a} \rangle \ll \frac{\Delta_R^2}{\lambda^2}$ [32]. In this limit, the Hamiltonian can be approximated in rotating coordinates as

$$\frac{H_{disp}^{qm}}{\hbar} = \left(\omega_m + \frac{\lambda^2}{4\Delta_R} \hat{\sigma}_z \right) \hat{a}^\dagger \hat{a} + \frac{1}{2} \Omega_R \hat{\sigma}_z + \frac{\lambda^2}{8\Delta_R} \sigma_z. \quad (6)$$

Equation (6) illustrates, that in the dispersive regime, the mechanical resonance frequency gets shifted by $\pm \frac{\lambda^2}{4\Delta_R}$ where "+" and "-" correspond to the spin-qubit in the state $|\uparrow\rangle$ and $|\downarrow\rangle$, respectively. Optically measuring the shift of the mechanical frequency allows readout for the spin state via the mechanical resonator similarly to how monitoring the resonance frequency of a waveguide resonator is used for reading out the coupled superconducting qubit [29, 33]. Furthermore, the interaction term

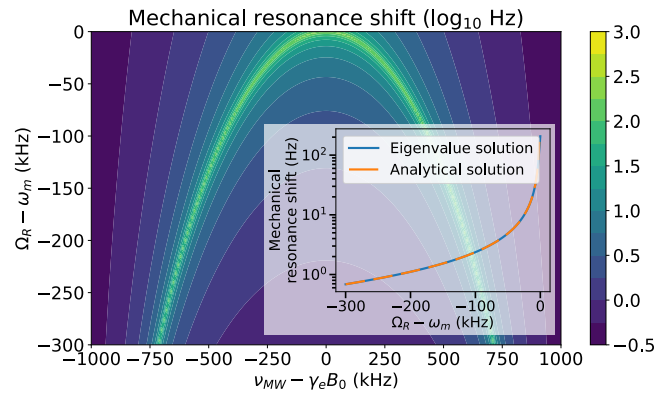


FIG. 2: The expected shift of the mechanical resonance frequency as function of the detunings in our system. These shifts were calculated from the energy levels of the qubit-oscillator Hamiltonian, and thus no linewidths have been implemented for the qubit or the resonator. The simulation shows an interplay between the detunings: the maximal shift follows well the qubit-mechanics resonance condition $\omega_m = \sqrt{\Omega_R^2 + \Delta\nu^2}$. The inset shows a linecut at $\nu_{MW} - \gamma_e B_0 = 0$, together with an analytical calculation for the expected shift $\Delta\omega_m = \lambda^2 \Omega_R / [2(\omega_m^2 - \Omega_R^2)]$ [34]. For the numerical values here, we have fixed the coupling strength as $\lambda = 1$ kHz, and $\omega_m = 1$ MHz.

$\frac{\lambda^2}{4\Delta_R} \hat{\sigma}_z \hat{a}^\dagger \hat{a}$ in Eq. (6) commutes with the local Hamiltonians of the qubit and the mechanical resonator, and thus the readout is a non-demolition measurement, leaving the qubit state unchanged.

Note also that the criterion for the the dispersive regime $\langle \hat{a}^\dagger \hat{a} \rangle \ll \frac{\Delta_R^2}{\lambda^2}$ effectively sets the temperature range of the readout: Higher expectation value for the phonon number means that larger detuning must be used to satisfy the condition. Increasing the detuning, in turn, diminishes the expected frequency shift. Otherwise the thermal state of the resonator here does not necessarily matter as in the dispersive regime it does not lead to the thermalization of the qubit state.

B. Numerical simulation

The approximated Hamiltonian in Eq. (6) shows that the readout works in the noiseless scenario and when both the RWA and dispersive assumptions are satisfied. Now, we numerically benchmark our system in a more realistic noisy environment and test how much compromising the RWA and dispersive assumptions affects the readout. We relax any assumptions concerning RWA and the dispersive limit in our model and apply the general qubit-mechanics Hamiltonian in Eq. (3). Since in our experimental implementation smaller Rabi frequencies are easier to implement, we restrict here to the regime where $\Omega_R \leq \omega_m$.

Figure 2 illustrates the shift of the energy level spacing

of the qubit-mechanics Hamiltonian in Eq. (3) as function of the Rabi and Zeeman detunings. The simulation shows that when the natural mechanical resonance frequency ω_m is comparable to the driven qubit's eigenfrequency, or in other words $\omega_m \approx \sqrt{\Omega_R^2 + \Delta\nu^2}$, we expect a shift of the mechanical resonance frequency that depends on the spin state. The eigenvalue simulation shows also, that the shift is maximized in resonant driving, namely when $\Delta\nu = 0$ and $\Omega_R \approx \omega_m$.

Next, we want to consider the dynamics of the system including finite linewidths for the qubit and the mechanical resonator and noting that the mechanical resonator might initially be in a thermal state. We use the Python Qutip [35, 36] package to numerically study the relation between the mechanical frequency shift, the detunings and the coupling strength λ using Eq. (3) to model the dynamics. The aim of the simulations is to find the minimal spin-mechanics coupling strength leading to successful spin readout via the optomechanical quantum bus and to analyze the performance of different coupling mechanisms and designs. Here we define the readout to be reliable if the spin-dependent shift of the mechanical frequency is at least as large as the mechanical linewidth, which for our simulations and measured devices is 200 Hz. We note that the 200 Hz shift discussed here is a pessimistic requirement: Optomechanical self-oscillations can be used to narrow the mechanical linewidth, leading to higher precision of an optomechanical force sensor [37]. Furthermore, notably smaller shifts can be detected using an optomechanical lock-in measurement.

In the numerical simulations, the linewidths are implemented by introducing decay channels for the qubit and mechanical resonator with the Gorini-Kossakowski-Sudarshan-Lindblad (GKSL) master equation

$$\frac{d\hat{\rho}}{dt} = i \left[\hat{\rho}, \hat{H}_\rho^{qm} \right] + \sum_{k=1}^4 \kappa_k \left[\hat{A}_k \hat{\rho} \hat{A}_k^\dagger - \frac{1}{2} \left(\hat{A}_k^\dagger \hat{A}_k \hat{\rho} + \hat{\rho} \hat{A}_k^\dagger \hat{A}_k \right) \right] \quad (7)$$

where \hat{A}_k are the jump operators corresponding to the decay channels and κ_k are their decay rates. In our case, $\hat{\rho}$ is the density matrix of the total qubit-mechanics system, the jump operators are $\hat{A}_1 = \hat{a}$, $\hat{A}_2 = \hat{a}^\dagger$ for the dissipation and heating of the mechanical resonator, $\hat{A}_3 = \hat{\sigma}_-$, $\hat{A}_4 = \hat{\sigma}_+$ for the qubit T_1 process, and $\hat{A}_5 = \hat{\sigma}_z$ for the qubit T_2 process, and the unitary part is governed by the dressed qubit-phonon Hamiltonian \hat{H}_ρ^{qm} in Eq. (3). The decay rates κ_k are chosen so that the linewidths of the resulting noise spectral densities of the uncoupled dressed qubit T_1 and T_2 processes and the mechanical resonator correspond to their measured values in the practical implementation we describe later in Sec. V; $1/T_1 = 10$ Hz [6], $1/T_2 = 100$ Hz [6], and mechanical linewidth of 200 Hz.

From the solution of the master equation Eq. (7), we calculate the symmetrized spectral density $\bar{S}_{\hat{X}\hat{X}}(\omega) :=$

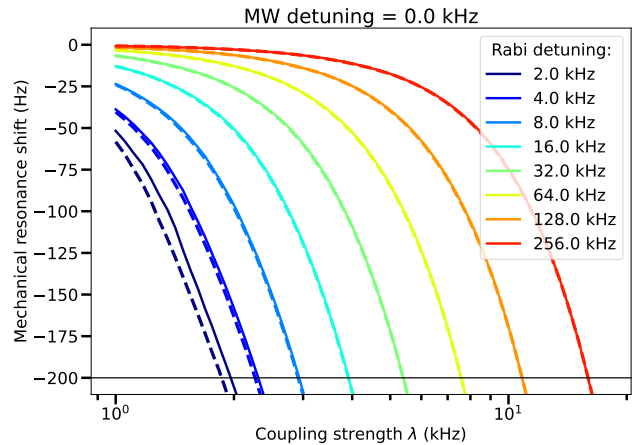


FIG. 3: Shift of the mechanical frequency as function of the coupling strength for different detunings between the mechanical resonator and the qubit's Rabi frequency, which effectively define the possible operation temperature. Here, $\omega_m = 1$ MHz. The horizontal black line corresponds to the assumed mechanical linewidth of 200 Hz. The solid and dashed lines correspond to the mechanical resonator initialized in the thermal state ($n_{th} = 3$) and ground state, respectively.

$[S_{\hat{X}\hat{X}}(\omega) + S_{\hat{X}\hat{X}}(-\omega)]/2$. Here

$$S_{\hat{X}\hat{X}}(\omega) = \int_{-\infty}^{+\infty} \langle \hat{X}(t) \hat{X}(0) \rangle e^{i\omega t} dt, \quad (8)$$

is the noise spectral density of the mechanical resonator, $\hat{X} = (\hat{a}^\dagger + \hat{a})$ is the displacement operator of the mechanical resonator, and $\langle \rangle$ corresponds to the expectation value. Then, the shifted mechanical frequency is determined from $\bar{S}_{\hat{X}\hat{X}}(\omega)$ for different coupling strengths λ and detunings.

An example plot of the calculated mechanical frequency shifts is presented in Fig. 3. We have done the simulation with the mechanical resonator ($\omega_m = 1$ MHz) both in the ground state and with a small thermal population $n_{th} = 3$. We see that the results for these two starting states differ for small Rabi detunings, highlighting the fact that a thermal state will not prevent the spin readout protocol, but it will shift the required Rabi detuning to be in the dispersive regime.

The simulation is repeated for different values of MW detuning to study its effect on the readout. Fig. 4 shows the crossover values leading to the required mechanical frequency shift of 200 Hz - the magnitude of mechanical linewidth - for each detuning combination for the initial state with $n_{th} = 3$. At high Rabi detunings we see consistency with the simple eigenstate calculation of Fig. 2 for both $n_{th} = 0$ and $n_{th} = 3$ and all MW detunings. There is no notable difference between the resonant MW drive and the 10 kHz MW detuning. As expected, the results deviate notably from the prediction of the dispersive

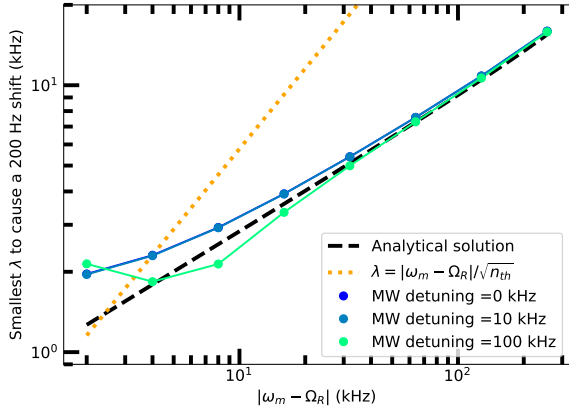


FIG. 4: Smallest coupling strength λ to cause the 200 Hz shift of mechanical frequency for different combinations of MW and Rabi detunings. Dashed black line shows the expected Jaynes-Cummings behaviour $\Delta\omega_m = \lambda^2\Omega_R/[2(\omega_m^2 - \Omega_R^2)]$ [34]. Dotted yellow line marks roughly the dispersive limit boundary. Here $n_{th} = 3$.

regime for small Rabi detunings in all cases. For a moderate MW detuning of 100 kHz we see that the results don't match the resonant case. Interestingly, at intermediate Rabi detunings the 200 Hz mechanical frequency shift is now reached at smaller λ . This is in line with the eigenvalue simulation in Fig. 2 which reflects the combined roles of Ω_R and $\Delta\nu$ in the driven qubit's eigenfrequency and thus its resonance conditions with the mechanical resonator. This can be useful in cases where inducing high Rabi frequency has undesired effects, such as sample heating caused by the high MW power the large B_1 requires: detuning the MW drive allows more pronounced mechanical shift at lower Ω_R without needing a larger λ which is harder to tune. We also see a good match between the analytical solution at the dispersive limit and the simulated full dynamics at higher Rabi detunings for both the small and the moderate MW detunings.

In Sec. V A, we will discuss how large coupling strengths can be expected from our current and proposed optimized device designs and how well they can perform in the spin-qubit readout.

IV. SPIN-SPIN COUPLING VIA THE PHONON SYSTEM

Exploiting an intermediary quantum system has proven useful for implementing controlled 2-qubit gates for other physical implementations of a qubit: Two double quantum dots were coupled via MW line integrated on the chip [38]. Coupling two superconducting qubits via an MW transmission line was experimentally demonstrated in [39, 40] and entangling qubits via a mechanical oscillator has been considered theoretically for NV cen-

$$\begin{aligned} |\downarrow\downarrow\rangle &\xrightarrow{\sqrt{iSWAP}} |\downarrow\downarrow\rangle \\ |\downarrow\uparrow\rangle &\xrightarrow{\sqrt{iSWAP}} \frac{1}{\sqrt{2}} (|\downarrow\uparrow\rangle + i|\uparrow\downarrow\rangle) \\ |\uparrow\downarrow\rangle &\xrightarrow{\sqrt{iSWAP}} \frac{i}{\sqrt{2}} (|\downarrow\uparrow\rangle - i|\uparrow\downarrow\rangle) \\ |\uparrow\uparrow\rangle &\xrightarrow{\sqrt{iSWAP}} |\uparrow\uparrow\rangle \end{aligned}$$

TABLE I: The two-qubit gate \sqrt{iSWAP} turns the product states $|\downarrow\uparrow\rangle$ and $|\uparrow\downarrow\rangle$ into maximally entangled states. In combination with single qubit unitary operations, \sqrt{iSWAP} forms the universal gate set.

ters in diamond in [41] and similarly for atoms in optical cavities in [42].

A. Dispersive limit

Let us consider, what happens when two donor spin qubits are coupled to the same mechanical resonator but don't interact directly with each other. The total qubit-mechanics-qubit Hamiltonian can be written in the dressed frame as

$$\frac{\hat{H}_\rho^{qmq}}{\hbar} = \omega_m \hat{a}^\dagger \hat{a} + \frac{1}{2} \sum_{k=1}^2 \Omega_R^k \hat{\sigma}_z^k + \Delta\nu^k \hat{\sigma}_x^k - \lambda^k \hat{\sigma}_x^k (\hat{a}^\dagger + \hat{a}), \quad (9)$$

where the superscript $k \in \{1, 2\}$ labels the qubits 1 and 2.

Now, to provide intuition on how and why the quantum bus can implement entangling 2-qubit gates, we follow the approach presented in [29, 43]: By performing the RWA and taking the dispersive limit $\lambda^k \ll 2|\Omega_R^k - \omega_m|$, we can approximate the combined Hamiltonian as

$$\begin{aligned} \frac{\hat{H}_{disp}^{qmq}}{\hbar} &= \left[\omega_m + \sum_{j=1}^2 \frac{(\lambda^j)^2}{4(\Omega_R^j - \omega_m)} \sigma_z^j \right] \hat{a}^\dagger \hat{a} \\ &+ \frac{1}{2} \sum_{k=1}^2 \left[\left(\Omega_R^k + \frac{(\lambda^k)^2}{4(\Omega_R^k - \omega_m)} \right) \hat{\sigma}_z^k + \Delta\nu^k \hat{\sigma}_x^k \right] \\ &+ \frac{\lambda^1 \lambda^2 (\Omega_R^1 - \omega_m + \Omega_R^2 - \omega_m)}{8(\Omega_R^1 - \omega_m)(\Omega_R^2 - \omega_m)} (\hat{\sigma}_+^1 \hat{\sigma}_-^2 + \hat{\sigma}_-^1 \hat{\sigma}_+^2). \end{aligned} \quad (10)$$

In this noiseless dispersive case, the interaction term of the Hamiltonian Eq. (9) results in the \sqrt{iSWAP} gate between the two spin-qubits when the interaction time is $\frac{(\Omega_R^1 - \omega_m)(\Omega_R^2 - \omega_m)}{\lambda_1 \lambda_2 (\Omega_R^1 - \omega_m + \Omega_R^2 - \omega_m)}$. Table I shows how \sqrt{iSWAP} operates on the two-qubit basis states. The gate can be used to entangle the qubits and forms a universal gate set with unitary one-qubit gates.

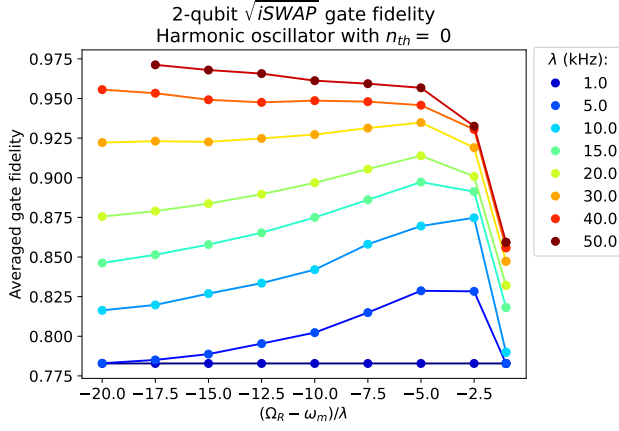


FIG. 5: The \sqrt{iSWAP} -gate fidelity as function of Rabi detuning and coupling strength.

B. Numerical simulation

Again, we perform numerical simulations to estimate how our quantum bus will perform in more realistic noisy environment. As in Sec. III, we relax all the assumptions concerning the dispersive limit and RWA to avoid their unnecessary influence on the results and use the Hamiltonian of Eq. (9).

We consider the situation where the dressed qubits are in resonance $\Omega_R^1 = \Omega_R^2 = \Omega_R$ and their coupling strengths are equal $\lambda_1 = \lambda_2 = \lambda$. In this case the dispersive regime's ideal interaction time to implement the \sqrt{iSWAP} gate becomes $\frac{1}{2\lambda} \frac{\Omega_R - \omega_m}{\lambda}$. We see two competing roles for the parameters: the larger the λ or the $\frac{\lambda}{\Omega_R - \omega_m}$ is, the faster the gate becomes. Simultaneously, increasing either of these terms pushes us further away from the dispersive regime $\lambda \ll 2|\Omega_R - \omega_m|$, and the assumptions used to get to the Hamiltonian in Eq. (10) are not valid anymore. This emphasizes the importance of the Rabi detuning in implementing the 2-qubit gate under realistic noisy conditions: since the Markovian decoherence of the qubits in Eq. (7) leads to monotonic loss of information, quick gate implementation is desirable. On the other hand, only increasing the coupling strengths violates the underlying assumptions and hinders the gate implementation. Therefore, the Rabi-detuning must be increased to remain in the dispersive regime while increasing λ to make the gate fast enough to beat the decoherence.

We use again the GKSL master equation to implement the decoherence processes for the two qubits and the mechanical resonator to simulate the dynamics of the two-qubit system like in Sec. III. We use two (virtual) ancillary qubits that don't interact with each other or the other systems to construct the Choi matrix of the original 2-qubit system by using the Choi–Jamiołkowski isomorphism. The Choi matrix fully captures the implemented two-qubit gate for any input state and it allows

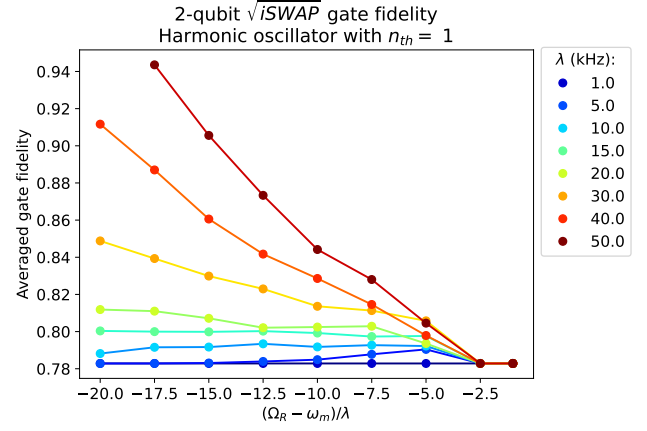


FIG. 6: Effects of finite mechanical resonator temperature to the \sqrt{iSWAP} -gate fidelity.

a straightforward way to calculate the averaged gate fidelity between the target gate – \sqrt{iSWAP} – and the dynamical map which we get as the numerical solution of the master equation.

The dynamical map consists of a time-parametrized family of quantum channels Φ_t for all time points of the simulation t . The averaged gate fidelity is defined as the quantity

$$\mathcal{F}_{\Phi_t, U}(\phi) := \left(\text{tr} \left[\sqrt{\sqrt{\Phi_t(\phi)} U(\phi) \sqrt{\Phi_t(\phi)}} \right] \right)^2 \quad (11)$$

averaged over all initial states ϕ . In [44] it was shown that the averaged gate fidelity can be written as

$$\mathcal{F}_{\Phi, U} = \frac{d + \sum_n \text{tr} [K_n U^\dagger] \text{tr} [K_n^\dagger U]}{d^2 + d}. \quad (12)$$

Here $U(\rho) = U\rho U^\dagger$ is the target unitary gate to be implemented, d is the Hilbert space dimension of the input and output of the implemented channel Φ , and $\{K_n\}_n$ is any set of Kraus operators for Φ such that $\Phi(\rho) = \sum_n K_n \rho K_n^\dagger$ for any initial state ρ . After constructing the Choi matrix, we convert it into a corresponding set of Kraus operators and calculate the channel fidelity as in Eq. (12). The same is repeated for all interaction times and detuning-coupling strength combinations.

In Fig. 5 we present the simulated gate fidelity with different coupling strengths and Rabi detunings with the resonator initially in the ground state, and in Fig. 6 with the resonator initialized to one thermal phonon population. The gate fidelity value is picked at the optimal interaction time found separately in the simulation for each detuning-coupling pair. As expected, the qubit and resonator linewidths in our master equation and the deviation from the dispersive assumption lead to optimal times that differ from the analytical expression above. For small coupling strengths, we see that the fidelity is

not monotonic with Rabi detuning. This is explained by the competing effects of the dispersive assumption and the decoherence: Increasing the $|\Omega_R - \omega_m|/\lambda$ term on the interval $[0,5]$ brings the system further to the dispersive regime. Beyond that, increasing detuning makes the interaction slower than decoherence, therefore decreasing the gate fidelity. It is clear that high gate fidelities can still be achieved in the $n_{th} = 0$ case at higher Rabi detunings and λ . This is because in that regime the interaction is faster than the decoherence and the large Rabi detuning allows obeying the dispersive assumption. This makes the gates slower, but the simulations show that this is not yet a limiting factor at the expected decoherence rates. More studies are still needed to extrapolate this to higher temperatures.

Finally, we studied the effect of decreasing the decoherence on the \sqrt{iSWAP} gate. In Fig. 7, we present the gate fidelity as function of the total amount of open system decoherence for selected parameter pairs $\lambda, (\Omega_R - \omega_m)$ from Fig. 5. Here, all the κ_k decay rates are multiplied with the same coefficient $\gamma\%$. Here, $\gamma\% = 1$ corresponds to the linewidths used in the other simulations of this paper and $\gamma\% = 0$ is the noiseless case. We see that for these parameter pairs, we can implement high-fidelity gate when the coupling strength λ is sufficiently large and the qubit and mechanical resonator linewidths are small, and decreasing the linewidths has a large effect on the fidelity especially for smaller λ .

An alternative way to entangle the qubits is by post-selection after measuring the shift of the mechanical resonance frequency caused by two qubits at the opposite ends of the nanobeam [41]. Also the MW drive we apply to dress the qubits can be frequency modulated to implement the CNOT and $iSWAP$ gates depending on how the modulation parameters are chosen [45]. These approaches are more complex to implement experimentally than the method we have numerically analyzed here, since the former depends on measuring the mechanical resonator and the latter relies on MW modulation. Future work will show if the added complexity of these alternatives can lead to higher gate fidelities.

Next, we will introduce the current and optimized device geometries of our proposed quantum bus. From now on, we will concentrate on the achievable coupling strengths of different device designs.

V. CONCRETE IMPLEMENTATION

The specific implementation of the optomechanical quantum bus we propose is a modified version of the sliced silicon nanobeam introduced in Refs. [28, 46, 47]. The design starts with a silicon nanobeam that works as a waveguide for light. A periodic hole pattern is introduced to the waveguide, and causes a spatially altering refractive index that basically forms a Bragg reflector (1D photonic crystal). A defect in the periodicity of the holes at the waveguide's center allows optical frequencies inside the

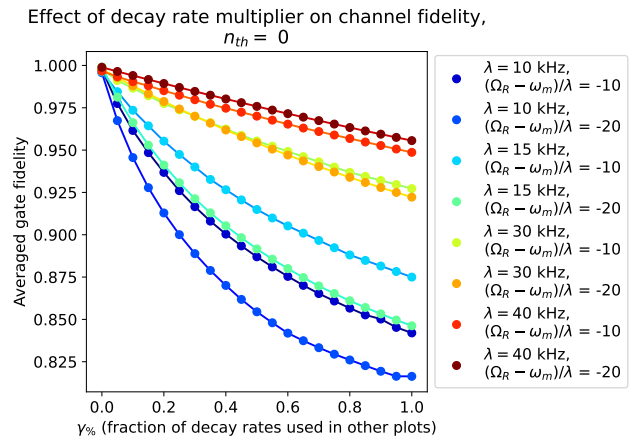


FIG. 7: The effect of decoherence on the \sqrt{iSWAP} -gate fidelity. Here, the horizontal axis is a front factor multiplying all the decay rates κ_k in our master equation. $\gamma\% = 100$ corresponds to the qubit linewidths $1/T_1 = 10$ Hz, $1/T_2 = 100$ Hz, and mechanical linewidth of 200 Hz used in our other simulations. $\gamma\% = 0$ corresponds to noiseless case

Bragg mirror's bandgap travel there and thus the defect works as an optical cavity. The mechanical displacement from the nanobeam halves moving with respect to each other modifies the resonance frequency of the optical cavity. This causes modulation in optical phase quadrature at the mechanical frequency ω_m , and therefore the interaction between the optical and mechanical modes is described by the standard optomechanical Hamiltonian in Eq. (5). Isotopically purifying the top layer of the device will prolong the qubit's lifetime [5], and in our experiments it has not been found to negatively impact the optical or mechanical properties of the devices (unpublished).

The mechanical resonance frequency of these devices is in the 1-10 MHz range, which allows bringing the dressed qubit into resonance with the mechanical resonator with reasonable MW powers. The linewidth of the optical cavity is orders of magnitude larger than the mechanical frequency ($\sim 10 - 100$ GHz). This means that the outgoing light information reflects the instantaneous mechanical position, which can be used for measurement based feedback cooling [48–50] and pulsed measurements [47, 51, 52]. Feedback cooling will be needed to bring these low frequency resonators close to their quantum ground state, where as pulsed measurements allow detecting short-lived shifts in the mechanical frequency and give a single-shot spin readout method.

In the following sections we will present spin-mechanics coupling mechanisms that can be utilized for silicon nanobeam quantum bus. Also the strengths and weaknesses of both methods will be analyzed.

A. The spin-phonon coupling strengths

As outlined in section II A the coherent spin-phonon coupling strength in the dressed frame is given by the change of the bare spin qubit resonance frequency by a displacement x_{zpf} . In our proposed platform, we consider two mechanisms to achieve this, both with their own strengths: motion-induced strain in the silicon lattice and a magnetic field gradient in the proximity of a micromagnet.

Both of these methods produce coupling strengths that vary heavily based on donor location, requiring precise control of donor placement for strong coupling. This can be achieved through deterministic ion implantation, where donors are placed in precisely determined locations using either a mask [25, 27] or an extremely precise focused ion beam [26].

Earlier, strain has been used to couple an optomechanical system to the electron spin of an NV center in diamond to optically control of the spin with a telecom wavelength laser [53]. On the other hand, micromagnets have been used to couple the electron spin in an NV center in diamond to the mechanical motion [54, 55]. Furthermore, resonantly driving an InAs quantum dot was shown to actuate the mechanical motion of a GaAs microwire via state-dependent strain [56]. Periodically modulating strain at the spin location has been experimentally shown to drive the electron spin of an NV center in diamond using electrically controlled high-overtone bulk acoustic resonator (HBAR) [57] and a piezoelectrically driven mechanical cantilever [58].

Next, we will discuss these coupling mechanisms in our proposed quantum bus design and estimate with numerical simulations the spin-mechanics coupling strengths they can provide.

1. Strain caused by the mechanical motion

The mechanical displacement deforms the silicon's crystal lattice surrounding the donor atom, shifting the surrounding silicon atoms closer or further from it, thus changing the background charge environment of the loosely bound donor electron (the electron wavefunction covers several tens of silicon atoms). As a consequence, the electron's effective g factor and the hyperfine interaction between the donor nucleus and electron change, resulting in a shift of the electron spin energy states. Until quite recently, the strain-induced shift was thought to be quadratic in strain as the valley repopulation theory [59] predicts, but it was in 2018 experimentally shown to be linear for small strains [60]. As the coupling strength is given by the strain that the donor experiences, the device geometry can be optimized by concentrating the amount of strain in a small region of the silicon crystal. The strain-induced change in the donor electron's spin resonance frequencies were reported to be 140 GHz/strain and 22 GHz/strain for phosphorus and bismuth, respec-

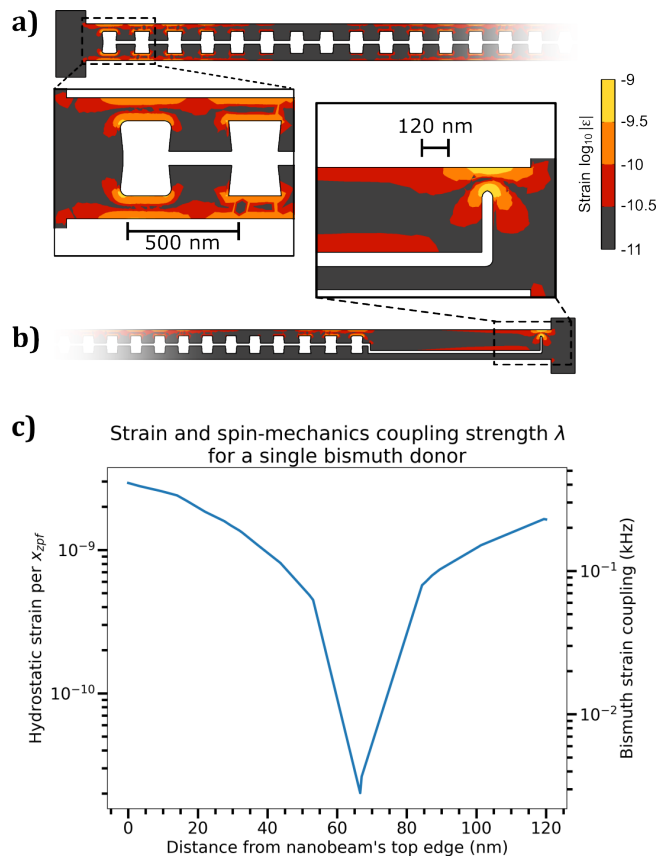


FIG. 8: Strain as spin-mechanics coupling. FEM simulation of the strain/ x_{zpf} for **a)** the original split nanobeam and **b)** the strain-optimized geometry. The insets emphasize the high-strain regions at the ends of the nanobeams. The strain is more concentrated at the split end and five times higher in the optimized geometry by adding a vertical slit. **c)** Spin-mechanics coupling strength in the strain-optimized geometry: The left y-axis shows the strain along the vertical linecut near the vertical split's end and the right y-axis if the corresponding spin-mechanics coupling strength for a single bismuth donor electron.

tively¹ [60]. Since any motion of the split nanobeam halves causes deformation in the silicon lattice, strain is a very appealing choice for the coupling mechanism as it does not require any additional fabrication steps.

Figure 8 shows the COMSOL FEM simulations of the strain distribution caused by the zero point fluctuation (x_{zpf}) motion for two device geometries: in Fig. 8a) similar to the devices used in [28, 46, 47], and in Fig. 8b) the strain-optimized geometry. We see that in the origi-

¹ The reported values for the lowest field transitions/corresponding to the nuclear spin in its ground state and the 90 degree angle between the static magnetic field and the silicon crystal [001] direction.

nal nanobeam geometry the high-strain areas are widely spread near the ends and the center of the nanobeam. Importantly, the added vertical slit in the optimized geometry spatially confines and increases the amount of the strain, which leads to a 5-fold enhancement for the spin-mechanics coupling strength. In the high-strain regions this optimized geometry provides coupling strengths of 60 Hz and 400 Hz for a single phosphorus and bismuth donor, respectively. The high-strain areas are near the narrow slits at both ends of the nanobeam, allowing use of the motion of the beam as a communication channel between two donor spins at the opposite ends as discussed in Sec. IV.

2. Magnetic field gradient of a micromagnet

Alternatively, we can couple the spin-qubit to the nanobeam's mechanical motion via the magnetic field gradient induced by a stationary on-chip micromagnet fabricated near the nanobeam's center. COMSOL simulation of the magnetic field gradient for one example magnet geometry in Fig. 9 a) illustrates how the magnetic field gradient changes less drastically along the nanobeam, and thus the required donor implantation precision is set by the distance across the nanobeam.

When the nanobeam moves the distance Δx towards the magnet, a donor in the beam experiences a magnetic field gradient ∇B , modulating the Zeeman splitting of the electron by $\Delta x \nabla B \gamma_e$ which corresponds to the spin-mechanics coupling strength. The coupling rates for all donor species can thus be increased by maximizing both the distance traveled by the donor and the magnetic field gradient that the donor experiences.

To maximize simulataneously both Δx and ∇B , the donor can be implanted at the center of the nanobeam where the beam's displacement is maximal, and the micromagnet should be placed near the donor, since ∇B is strongest near the magnet. Split silicon nanobeams with device geometries similar to ours have been reported to have x_{zpf} values of 43 fm [28] and 80 fm [46]. Still, x_{zpf} can be enhanced with design changes: Lower mechanical resonance frequency should lead to floppier devices with higher x_{zpf} , as $x_{zpf} = \sqrt{\hbar/2m_{eff}\omega_m}$, and lengthening the beam will decrease the mechanical resonance frequency ω_m more than it increases the effective mass m_{eff} . Furthermore, the magnetic field gradient ∇B can be increased by optimizing the magnet geometry, thickness, proximity, and material. The effects of proximity to ∇B and the resulting spin-mechanics coupling strength λ for a single phosphorus donor are shown in Fig. 9 b) for a selection of magnet thicknesses. We see that increasing the magnet thickness beyond 100 nm does not notably change the the magnetic field gradient.

For a phosphorus donor in silicon, the Zeeman splitting obeys the linear relation of 28 GHz/T at relatively small fields, making the relationship between ∇B and the coupling simple. On the other hand, for bismuth, the

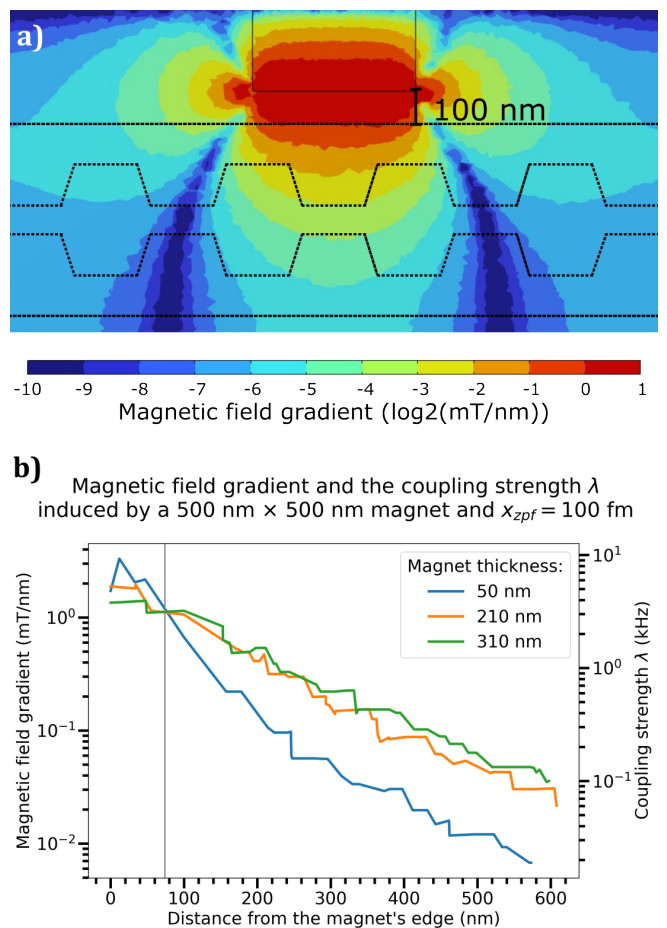


FIG. 9: Micromagnet induced magnetic field gradient for spin-mechanics coupling. **a)** COMSOL FEM simulation of the 2D spatial distribution of the magnetic field gradient caused by a micromagnet with dimensions of $500 \text{ nm} \times 500 \text{ nm} \times 300 \text{ nm}$ (length \times width \times height). The dotted line shows approximate position of the silicon nanobeam. **b)** COMSOL FEM simulation of the magnetic field gradient at the center of the nanobeam as function of the distance from the magnet's edge (left y-axis), and the resulting spin-mechanics coupling strength for a single phosphorus donor electron (right y-axis), where we have used $x_{zpf} = 100 \text{ fm}$ and a square $500 \text{ nm} \times 500 \text{ nm}$ magnet. For similar resonators, $x_{zpf} = 80 \text{ fm}$ was determined by Leijssen *et al* [46].

nuclear spin of 9/2 creates a more complex energy level system, whose Zeeman splitting is nonlinear with respect to magnetic field at low fields, as shown in Fig. 10. At the lowest field transition, the coupling strength for a bismuth donor is 7% less than for a phosphorus donor and for the higher nuclear spin transitions it is even weaker.

Therefore, the optimal choice of the donor species depends on the used coupling mechanism: While bismuth donors give rise to nearly ten-fold greater coupling strengths for strain coupling, phosphorus is superior for magnetic field gradient coupling. We note that the cou-

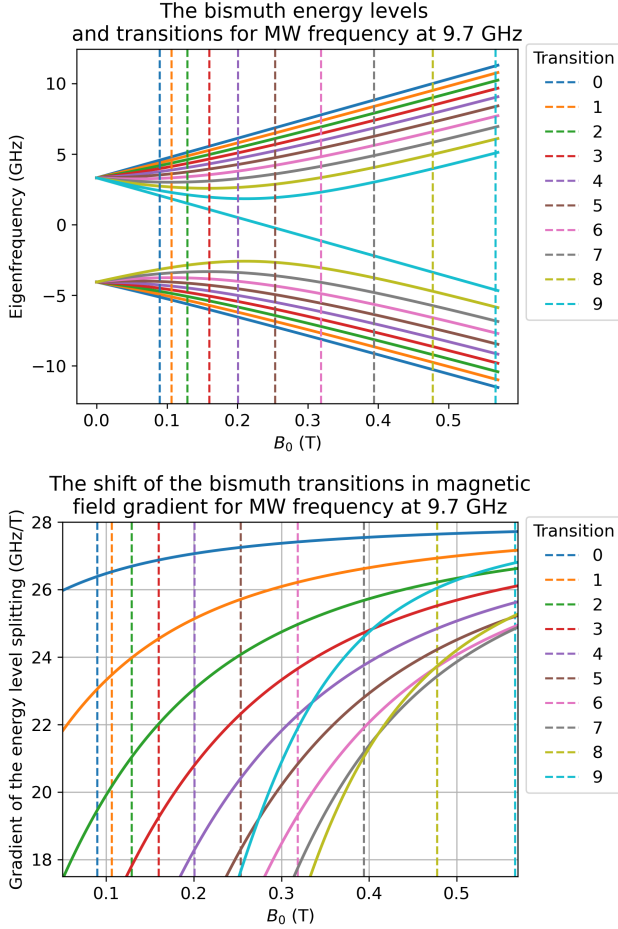


FIG. 10: **Top:** Bismuth donor electron energy level diagram. The dashed lines illustrate the magnetic fields corresponding to Zeeman splitting between the matching colored energy levels at 9.7 GHz. The lowest field transition, labeled as "0", provides the strongest spin-mechanics coupling via strain [60]. **Bottom:** Gradient of the bismuth Zeeman splitting for all the nuclear spin states. The gradient varies a lot between the different transitions and it is not constant even at relatively high fields.

pling strength for a single phosphorus donor with magnetic field gradient coupling is an order of magnitude higher than for strain coupling for a single bismuth donor, making magnetic field gradient coupling with a phosphorus donor the better option for single spin readout. On the other hand, the area of active donor coupling is limited only to the center of the nanobeam and the inclusion of a metal micromagnet increases fabrication complexity.

3. The performance of the proposed device designs

Now, let us combine the COMSOL simulations with the Qutip simulations in Sec. III and compare how well

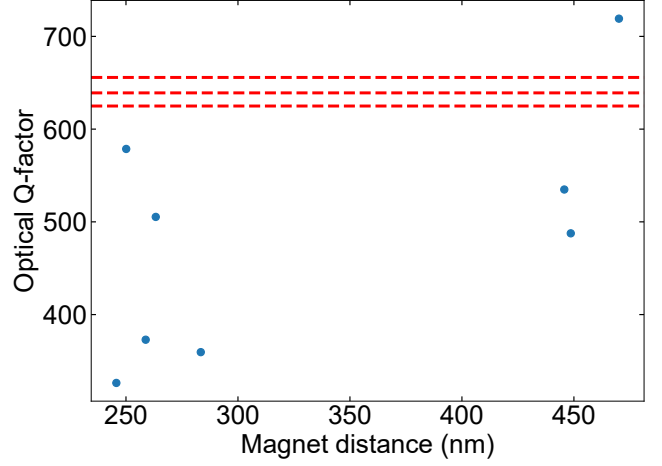


FIG. 11: The optical Q-factors (ω_c/κ) of optomechanical resonators as a function of the closest distance between beam and magnet (blue dots) as well as of magnet-free control samples (red dashed lines). Here the control samples optical quality was not at high as in previous demonstration due to non-ideal lithography. This still shows a definite lower bound for the achievable optical quality factor with the micromagnet.

the different proposed device will perform for the spin-qubit readout. When $\Delta_R \geq 4$ kHz, we see from Fig. 4 that coupling strength of 3 kHz is enough for a successful spin-qubit readout and there $\lambda < \Delta_R$. The simulated coupling from the magnetic field gradient of a 310 nm thick magnet in Fig. 9 shows that $\lambda = 3$ kHz is easily reached with implantation precision of 50 nm from the nanobeam's top edge, which is within the reach of current ion implantation technologies. Thus, the magnetic field gradient coupling is strong enough for single-donor readout within the current fabrication capabilities.

On the contrary, even for the optimized strain coupling device geometry the single-donor coupling strength is at most 0.4 kHz, which is much less than what is needed for the qubit readout. On the other hand, we can consider the readout of an ensemble spin of multiple of donors confined in the same high-strain region. According to the Tavis-Cummings model, if the coupling strength between a qubit and a harmonic oscillator for a single qubit is λ_1 , then the coupling strength between the ensemble spin of n qubits and the harmonic oscillator is $\lambda_n = \sqrt{n}\lambda_1$. Thus, the strain coupling of the optimized geometry is strong enough to read out the ensemble spin state of 225 bismuth donors implanted within the high-strain region of $30 \times 30 \times 80$ (nm)³, where $\lambda \geq 0.2$ kHz.²

Concerning the optomechanical readout of the spin-

² Considering here donors uniformly distributed in the isotopically purified layer of 80 nm. The width of the high-strain area is estimated notably downwards, since in the x direction the strain distribution is wider than in y, which is what we have in the line-

qubits, it should be noted that metal magnets have a large imaginary component to their refractive indices, leading to significant absorption. If this impacts the optical cavity mode notably, it could be detrimental to the optical readout. To test this, we have experimentally fabricated a series of optomechanical cavities in close proximity to nickel micromagnets and performed measurements to characterize their optical and mechanical resonances. There were no differences in the mechanical resonance between the magnet and control samples, nor in the optical resonance frequency ω_c . The presence of the micromagnet increased the optical linewidth κ and thus decreased the optical quality factor. The resonators that were closest to the magnet experienced the sharpest drop in quality, as seen in Fig. 11. Importantly, the optical cavity still survived the presence of the magnet and thus the micromagnet does not critically compromise the performance of the quantum bus. The observed Q-values were enough for high-quality optomechanical interface.

VI. OUTLOOK

We have presented a proposal for creating a new kind of quantum hybrid system that combines donor spins and optomechanical resonators in a silicon platform. The proposed device could work as both coupling pathway between spins and as an optical readout mechanism. Ultimately, also coherent coupling from the spins to photons

could be considered, but this was not our aim here.

The fact that our design relies on coherent coupling between a microwave *dressed* qubit and the mechanical resonator means that we are forced to work with relatively low frequency resonators in the MHz range, and hence need to carefully consider the effects of the thermal phonon population to the methods we propose. To avoid the effects of the thermal population, we aim to work in the non-resonant "dispersive" regime of the resonator-qubit interaction. For the readout, we show that the thermal population does not cause problems, as long as care is taken to stay well in the dispersive regime. This means higher phonon populations will require more detuning that then reduced the detected signal. The same applies for the two qubit gates: higher thermal phonon population requires higher Rabi detuning, making the gates slower. The limiting factor will be to keep the gate within the decoherence time of the qubits.

ACKNOWLEDGEMENTS

H. L. was funded by the European Research Council (ERC) under the European Union's Horizon 2020 research and innovation programme (Grant Agreement No. 852428). A. H. and T. H. were funded by the Finnish Quantum Flagship (project no. 210000621611). T. H. was funded by the Research Council of Finland project DYNCOR (project no. 354735).

-
- [1] B. E. Kane, A silicon-based nuclear spin quantum computer, *Nature* **393**, 133 (1998).
- [2] A. Morello, J. J. Pla, F. A. Zwanenbourg, K. W. Chan, K. Y. Tan, H. Huebl, M. Möttönen, C. D. Nugroho, C. Yang, J. A. van Donkelaar, A. D. C. Alves, D. N. Jamieson, C. C. Escott, L. C. L. Hollenberg, R. G. Clark, and A. S. Dzurak, Single-shot readout of an electron spin in silicon, *Nature* **467**, 687 (2010).
- [3] J. J. Pla, K. Y. Tan, J. P. Dehollain, W. H. Lim, J. J. L. Morton, D. N. Jamieson, A. S. Dzurak, and A. Morello, A single-atom electron spin qubit in silicon, *Nature* **489**, 541 (2012).
- [4] J. J. Pla, K. Y. Tan, J. P. Dehollain, W. H. Lim, J. J. L. Morton, F. A. Zwanenbourg, D. N. Jamieson, A. S. Dzurak, and A. Morello, High-fidelity readout and control of a nuclear spin qubit in silicon, *Nature* **496**, 334 (2013).
- [5] J. T. Muhonen, J. P. Dehollain, A. Laucht, F. E. Hudson, R. Kalra, T. Sekiguchi, K. M. Itoh, D. N. Jamieson, J. C. McCallum, A. S. Dzurak, and A. Morello, Storing quantum information for 30 seconds in a nanoelectronic device, *Nature Nanotechnology* **9**, 986 (2014).
- [6] A. Laucht, R. Kalra, S. Simmons, J. P. Dehollain, J. T. Muhonen, F. A. Mohiyaddin, S. Freer, F. E. Hudson, K. M. Itoh, D. N. Jamieson, J. C. McCallum, A. S. Dzurak, and A. Morello, A dressed spin qubit in silicon, *Nature Nanotechnology* **12**, 61 (2017).
- [7] J. T. Muhonen, A. Laucht, S. Simmons, J. P. Dehollain, R. Kalra, F. E. Hudson, S. Freer, K. M. Itoh, D. N. Jamieson, J. C. McCallum, A. S. Dzurak, and A. Morello, Quantifying the quantum gate fidelity of single-atom spin qubits in silicon by randomized benchmarking, *Journal of Physics: Condensed Matter* **27**, 154205 (2015).
- [8] B. Koiller, X. Hu, and S. Das Sarma, Exchange in Silicon-Based Quantum Computer Architecture, *Physical Review Letters* **88**, 027903 (2001).
- [9] M. T. Madzik, S. Asaad, A. Youssry, B. Joecker, K. M. Rudinger, E. Nielsen, K. C. Young, T. J. Proctor, A. D. Baczewski, A. Laucht, V. Schmitt, F. E. Hudson, K. M. Itoh, A. M. Jakob, B. C. Johnson, D. N. Jamieson, A. S. Dzurak, C. Ferrie, R. Blume-Kohout, and A. Morello, Precision tomography of a three-qubit donor quantum processor in silicon, *Nature* **601**, 348 (2022).
- [10] H. G. Stemp, S. Asaad, M. R. v. Blankenstein, A. Vaartjes, M. A. I. Johnson, M. T. Mądzik, A. J. A. Heskens, H. R. Firgau, R. Y. Su, C. H. Yang, A. Laucht, C. I. Ostrove, K. M. Rudinger, K. Young, R. Blume-Kohout, F. E. Hudson, A. S. Dzurak, K. M. Itoh, A. M. Jakob, B. C. Johnson, D. N. Jamieson, and A. Morello, Tomography of entangling two-qubit logic operations in exchange-coupled donor electron spin qubits, *Nature Communications* **15**, 8415 (2024).

plot in Fig. 8. Also, only one end of the nanobeam is assumed to be doped, when using both beam ends, 112.5 donors per the $30 \times 30 \times 80$ (nm)³ volume is enough.

- [11] G. Tosi, F. A. Mohiyaddin, V. Schmitt, S. Tenberg, R. Rahman, G. Klimeck, and A. Morello, Silicon quantum processor with robust long-distance qubit couplings, *Nature Communications* **8**, 450 (2017).
- [12] K. J. Morse, R. J. S. Abraham, A. DeAbreu, C. Bowness, T. S. Richards, H. Riemann, N. V. Abrosimov, P. Becker, H.-J. Pohl, M. L. W. Thewalt, and S. Simmons, A photonic platform for donor spin qubits in silicon, *Science Advances* **3**, e1700930 (2017).
- [13] A. Hijano, H. Lyyra, J. T. Muhonen, and T. T. Heikkilä, Characterization of a quantum bus between two driven qubits (2025), arXiv:2503.18772.
- [14] A. Laucht, F. Hohls, N. Ubbelohde, M. F. Gonzalez-Zalba, D. J. Reilly, S. Stobbe, T. Schröder, P. Scarlino, J. V. Koski, A. Dzurak, C.-H. Yang, J. Yoneda, F. Kuemmeth, H. Bluhm, J. Pla, C. Hill, J. Salfi, A. Oiwa, J. T. Muhonen, E. Verhagen, M. D. LaHaye, H. H. Kim, A. W. Tsen, D. Culcer, A. Geresdi, J. A. Mol, V. Mohan, P. K. Jain, and J. Baugh, Roadmap on quantum nanotechnologies, *Nanotechnology* **32**, 162003 (2021).
- [15] S. Barzanjeh, A. Xuereb, S. Gröblacher, M. Paternostro, C. A. Regal, and E. M. Weig, Optomechanics for quantum technologies, *Nature Physics* **18**, 15 (2022).
- [16] N. J. Lambert, A. Rueda, F. Sedlmeir, and H. G. L. Schwefel, Coherent Conversion Between Microwave and Optical Photons—An Overview of Physical Implementations, *Advanced Quantum Technologies* **3**, 1900077 (2020).
- [17] K. Stannigel, P. Rabl, A. S. Sørensen, M. D. Lukin, and P. Zoller, Optomechanical transducers for quantum-information processing, *Physical Review A* **84**, 042341 (2011).
- [18] A. Beccari, D. A. Visani, S. A. Fedorov, M. J. Breyhi, V. Boureau, N. J. Engelsen, and T. J. Kippenberg, Strained crystalline nanomechanical resonators with quality factors above 10 billion, *Nature Physics* **18**, 436 (2022).
- [19] E. A. Wollack, A. Y. Cleland, R. G. Gruenke, Z. Wang, P. Arrangoiz-Arriola, and A. H. Safavi-Naeini, Quantum state preparation and tomography of entangled mechanical resonators, *Nature* **604**, 463 (2022).
- [20] U. von Lüpke, Y. Yang, M. Bild, L. Michaud, M. Fadel, and Y. Chu, Parity measurement in the strong dispersive regime of circuit quantum acoustodynamics, *Nature Physics* **18**, 794 (2022).
- [21] A. Bassi, K. Lochan, S. Satin, T. P. Singh, and H. Ulbricht, Models of wave-function collapse, underlying theories, and experimental tests, *Reviews of Modern Physics* **85**, 471 (2013).
- [22] M. Carlesso, S. Donadi, L. Ferialdi, M. Paternostro, H. Ulbricht, and A. Bassi, Present status and future challenges of non-interferometric tests of collapse models, *Nature Physics* **18**, 243 (2022).
- [23] A. Bassi, A. Großardt, and H. Ulbricht, Gravitational decoherence, *Classical and Quantum Gravity* **34**, 193002 (2017).
- [24] P. M. Koenraad and M. E. Flatté, Single dopants in semiconductors, *Nature Materials* **10**, 91 (2011).
- [25] J. v. Donkelaar, C. Yang, A. D. C. Alves, J. C. McCallum, C. Hougard, B. C. Johnson, F. E. Hudson, A. S. Dzurak, A. Morello, D. Spemann, and D. N. Jamieson, Single atom devices by ion implantation, *Journal of Physics: Condensed Matter* **27**, 154204 (2015).
- [26] J. L. Pacheco, M. Singh, D. L. Perry, J. R. Wendt, G. Ten Eyck, R. P. Manginell, T. Pluym, D. R. Luhman, M. P. Lilly, M. S. Carroll, and E. Bielejec, Ion implantation for deterministic single atom devices, *Review of Scientific Instruments* **88**, 123301 (2017).
- [27] D. N. Jamieson, W. I. L. Lawrie, S. G. Robson, A. M. Jakob, B. C. Johnson, and J. C. McCallum, Deterministic doping, *Materials Science in Semiconductor Processing Advanced doping methods in semiconductor devices and nanostructures*, **62**, 23 (2017).
- [28] R. Leijssen, G. R. La Gala, L. Freisem, J. T. Muhonen, and E. Verhagen, Nonlinear cavity optomechanics with nanomechanical thermal fluctuations, *Nature Communications* **8**, ncomms16024 (2017).
- [29] A. Blais, R.-S. Huang, A. Wallraff, S. M. Girvin, and R. J. Schoelkopf, Cavity quantum electrodynamics for superconducting electrical circuits: An architecture for quantum computation, *Physical Review A* **69**, 062320 (2004).
- [30] M. Aspelmeyer, T. J. Kippenberg, and F. Marquardt, Cavity optomechanics, *Reviews of Modern Physics* **86**, 1391 (2014).
- [31] W. P. Bowen and G. J. Milburn, *Quantum optomechanics*, 1st ed. (CRC Press, 2015).
- [32] M. Boissonneault, J. M. Gambetta, and A. Blais, Dispersive regime of circuit QED: Photon-dependent qubit dephasing and relaxation rates, *Physical Review A* **79**, 013819 (2009).
- [33] A. Wallraff, D. I. Schuster, A. Blais, L. Frunzio, R.-S. Huang, J. Majer, S. Kumar, S. M. Girvin, and R. J. Schoelkopf, Strong coupling of a single photon to a superconducting qubit using circuit quantum electrodynamics, *Nature* **431**, 162 (2004).
- [34] E. K. Twyeffort Irish and K. Schwab, Quantum measurement of a coupled nanomechanical resonator-cooper-pair box system, *Phys. Rev. B* **68**, 155311 (2003).
- [35] J. Johansson, P. Nation, and F. Nori, QuTiP: An open-source Python framework for the dynamics of open quantum systems, *Computer Physics Communications* **183**, 1760 (2012).
- [36] J. Johansson, P. Nation, and F. Nori, QuTiP 2: A Python framework for the dynamics of open quantum systems, *Computer Physics Communications* **184**, 1234 (2013).
- [37] B. Guha, P. E. Allain, A. Lemaître, G. Leo, and I. Favero, Force sensing with an optomechanical self-oscillator, *Phys. Rev. Appl.* **14**, 024079 (2020).
- [38] F. Borjans, X. G. Croot, X. Mi, M. J. Gullans, and J. R. Petta, Resonant microwave-mediated interactions between distant electron spins, *Nature* **577**, 195 (2020).
- [39] M. A. Sillanpää, J. I. Park, and R. W. Simmonds, Coherent quantum state storage and transfer between two phase qubits via a resonant cavity, *Nature* **449**, 438 (2007).
- [40] J. Majer, J. M. Chow, J. M. Gambetta, J. Koch, B. R. Johnson, J. A. Schreier, L. Frunzio, D. I. Schuster, A. A. Houck, A. Wallraff, A. Blais, M. H. Devoret, S. M. Girvin, and R. J. Schoelkopf, Coupling superconducting qubits via a cavity bus, *Nature* **449**, 443 (2007).
- [41] E. Rosenfeld, R. Riedinger, J. Gieseler, M. Schuetz, and M. D. Lukin, Efficient Entanglement of Spin Qubits Mediated by a Hot Mechanical Oscillator, *Physical Review Letters* **126**, 250505 (2021).
- [42] A. S. Sørensen and K. Mølmer, Measurement Induced Entanglement and Quantum Computation with Atoms

- in Optical Cavities, *Physical Review Letters* **91**, 097905 (2003).
- [43] A. Blais, J. Gambetta, A. Wallraff, D. I. Schuster, S. M. Girvin, M. H. Devoret, and R. J. Schoelkopf, Quantum-information processing with circuit quantum electrodynamics, *Physical Review A* **75**, 032329 (2007).
- [44] E. Magesan, R. Blume-Kohout, and J. Emerson, Gate fidelity fluctuations and quantum process invariants, *Physical Review A* **84**, 012309 (2011).
- [45] V. Srinivasa, J. M. Taylor, and J. R. Petta, Cavity-mediated entanglement of parametrically driven spin qubits via sidebands (2023).
- [46] R. Leijssen and E. Verhagen, Strong optomechanical interactions in a sliced photonic crystal nanobeam, *Scientific Reports* **5**, 15974 (2015).
- [47] J. T. Muhonen, G. R. La Gala, R. Leijssen, and E. Verhagen, State preparation and tomography of a nanomechanical resonator with fast light pulses, *Physical Review Letters* **123**, 113601 (2019).
- [48] M. Rossi, D. Mason, J. Chen, Y. Tsaturyan, and A. Schliesser, Measurement-based quantum control of mechanical motion, *Nature* **563**, 53 (2018).
- [49] J. Guo, R. Norte, and S. Gröblacher, Feedback Cooling of a Room Temperature Mechanical Oscillator close to its Motional Ground State, *Physical Review Letters* **123**, 223602 (2019).
- [50] A. S. Kumar, J. Nätkinniemi, H. Lyyra, and J. T. Muhonen, Single-laser feedback cooling of optomechanical resonators (2022).
- [51] M. R. Vanner, I. Pikovski, G. D. Cole, M. S. Kim, C. Brukner, K. Hammerer, G. J. Milburn, and M. Aspelmeyer, Pulsed quantum optomechanics, *Proceedings of the National Academy of Sciences* **108**, 16182 (2011).
- [52] M. R. Vanner, J. Hofer, G. D. Cole, and M. Aspelmeyer, Cooling-by-measurement and mechanical state tomography via pulsed optomechanics, *Nature Communications* **4**, 2295 (2013).
- [53] P. K. Shandilya, D. P. Lake, M. J. Mitchell, D. D. Sukachev, and P. E. Barclay, Optomechanical interface between telecom photons and spin quantum memory, *Nature Physics* **17**, 1420 (2021).
- [54] O. Arcizet, V. Jacques, A. Siria, P. Poncharal, P. Vincent, and S. Seidelin, A single nitrogen-vacancy defect coupled to a nanomechanical oscillator, *Nature Physics* **7**, 879 (2011).
- [55] B. Pigeau, S. Rohr, L. Mercier de Lépinay, A. Gloppe, V. Jacques, and O. Arcizet, Observation of a phononic Mollow triplet in a multimode hybrid spin-nanomechanical system, *Nature Communications* **6**, 8603 (2015).
- [56] J. Kettler, N. Vaish, L. M. de Lépinay, B. Besga, P.-L. de Assis, O. Bourgeois, A. Auffèves, M. Richard, J. Claudon, J.-M. Gérard, B. Pigeau, O. Arcizet, P. Verlot, and J.-P. Poizat, Inducing micromechanical motion by optical excitation of a single quantum dot, *Nature Nanotechnology* **16**, 283 (2021).
- [57] E. R. MacQuarrie, T. A. Gosavi, N. R. Jungwirth, S. A. Bhave, and G. D. Fuchs, Mechanical Spin Control of Nitrogen-Vacancy Centers in Diamond, *Physical Review Letters* **111**, 227602 (2013).
- [58] A. Barfuss, J. Teissier, E. Neu, A. Nunnenkamp, and P. Maletinsky, Strong mechanical driving of a single electron spin, *Nature Physics* **11**, 820 (2015).
- [59] D. K. Wilson and G. Feher, Electron Spin Resonance Experiments on Donors in Silicon. III. Investigation of Excited States by the Application of Uniaxial Stress and Their Importance in Relaxation Processes, *Physical Review* **124**, 1068 (1961).
- [60] J. Mansir, P. Conti, Z. Zeng, J. Pla, P. Bertet, M. Swift, C. Van de Walle, M. Thewalt, B. Sklenard, Y. Niquet, and J. Morton, Linear Hyperfine Tuning of Donor Spins in Silicon Using Hydrostatic Strain, *Physical Review Letters* **120**, 167701 (2018).